An Integrated Converter and Machine Control System for MMC-Based High-Power Drives

Mauricio Espinoza-B., *Student Member, IEEE*, Roberto Cárdenas, *Senior Member, IEEE*, Jon Clare, *Senior Member, IEEE*, Diego Soto-Sanchez, *Member, IEEE*, Matias Diaz, *Student Member, IEEE*, Enrique Espina, *Student Member, IEEE*, and Christoph M. Hackl, *Senior Member, IEEE*

***Abstract*—The modular multilevel converter (MMC) is a promising topology for high-power drive applications. However, large voltage fluctuations can be produced in the floating capacitors when the machine operates with high stator currents at low rotational speed. To compensate these oscillations, relatively large mitigation currents are required to keep the capacitor voltages within an acceptable range. In this paper, a new integrated control scheme is discussed to regulate the voltage fluctuations. The strategy is based on closed-loop vector-control of the voltage fluctuations, maintaining them inside a predefined threshold. The proposed control system is also augmented using flux-weakening operation of the machine at low rotational speeds. An experimental prototype composed of 18 power cells, feeding a vector-controlled induction machine in the whole speed range, is used to validate the effectiveness and feasibility of the proposed control strategies.**

***Index Terms*—Flux-weakening operation, modular multilevel converter (MMC), variable speed drive, voltage balancing.**

Manuscript received July 30, 2017; revised December 18, 2017; accepted January 9, 2018. Date of publication February 5, 2018; date of current version October 31, 2018. This work was supported in part by FONDECYT under Grant 1140337, in part by the Advanced Centre for Electrical and Electronic Engineering, Basal Project FB0008, in part by CONICYT-PCHA/Doctorado Nacional /2014-63140233, and in part by the University of Costa Rica. *(Corresponding author: Roberto Cárdenas.)*

M. Espinoza-B. is with the Faculty of Engineering, University of Costa Rica, San Pedro 11501-2060, Costa Rica (e-mail: maeb@ieee.org).

R. Cárdenas and E. Espina are with the Department of Electrical Engineering, University of Chile, Santiago 8370448, Chile (e-mail: rcd@ieee.org; eespina@uchile.cl).

J. Clare is with the Faculty of Engineering, University of Nottingham, Nottingham NG7 2RD, U.K. (e-mail: jon.clare@nottingham.ac.uk).

D. Soto-Sanchez is with the Department of Electrical Engineering, University of Magallanes, Punta Arenas 6210427, Chile (e-mail: diego.soto@umag.cl).

M. Díaz is with the Department of Electrical Engineering, University of Santiago of Chile, Santiago 9170124, Chile (e-mail: matias.diazd@usach.cl).

C. M. Hackl is with the Munich University of Applied Sciences and Control of Renewable Energy Systems research group, Technical University of Munich, 80333 München, Germany (e-mail: christoph.hackl@hm.edu).

Color versions of one or more of the figures in this paper are available online at http://ieeexplore.ieee.org.

Digital Object Identifier 10.1109/TIE.2018.2801839

Nomenclature

Fonts

Scalar variables or symbols are indicated with italics (e.g., x), the complex vectors with bold (e.g., $\mathbf{x}$). Uppercase bold is used to represent real matrices (e.g., $\mathbf{X}$).

General

i	Current (A).
v	Voltage (V).
p	Power (W).
L	Inductance (H).
L_m	Mutual inductance (H).
L_r	Rotor inductance (H).
R	Resistance (Ω).
C	Capacitance (F).
τ_e	Electrical torque (Nm).
ω_e	Stator electrical frequency (rad·s^{-1}).
θ_e	Stator electrical angle (rad).
E	DC-port voltage (V).
n	Number of cells per cluster.
$f(t)$	Mitigating function with frequency ω_m.
$\mathbf{C}$	Matrix transformation.
$\mathbf{p}_{\omega_e}$	Power pulsation due to converter terminal variables.
$\mathbf{p}_m$	Power pulsation proportional to ω_e.
$\mathbf{p}_c$	Power pulsation due to circulating currents.

Superscripts

*	Set-point value of a variable.
^{X}	Electrical variable related with the terminal X of the MMC, $X \in \{P, N\}$.
$^\Sigma$, $^\Delta$	Variable in the ΣΔ-coordinate system.

Subscripts

$_\alpha$, $_\beta$, $_0$	Variable in the $\alpha\beta 0$-coordinate system.
$_d$, $_q$	Variable in the dq-coordinate system.
$_x$	Electrical variable related with the phase x of the MMC, $x \in \{a, b, c\}$.
$_C$	Electrical variable related to a capacitor.

Operators

$\tilde{}$	AC-component of a variable.
$\bar{}$	DC-component of a variable.
$\hat{}$	Unit vector.

0278-0046 © 2018 IEEE. Personal use is permitted, but republication/redistribution requires IEEE permission.
See http://www.ieee.org/publications_standards/publications/rights/index.html for more information.

^{c}	Complex conjugate of a complex vector.
$^\mathsf{T}$	Transpose of a matrix.
$\Re\{\ \}$	Real part calculator.

I. Introduction

SINCE the invention of the modular multilevel converter (MMC), it has been proposed for applications such as railway traction [1], [2], high-voltage dc transmission [3], [4] and machine drives [5]–[18]. Since this topology has several advantages when compared to other high-power converters (e.g., for quadratic torque-speed profile loads [6], [7]), a commercial solution based on the MMC has recently been made available in the market for medium-voltage drive applications [19]. However, significant efforts are still required to improve the performance of the control systems for MMC-based drives, particularly for some operating points where this topology is prone to instability [11].

A typical MMC topology to drive a cage induction machine is shown in Fig. 1. The converter is composed of six "clusters" connected to form a three-phase ac port and a dc port [see Fig. 1(a)]. Each cluster has an inductor L and n cascaded half-bridge cells. The energy in each cell is stored in a "flying" capacitor C [see Fig. 1(b)]. Consequently, satisfactory operation of an MMC requires a control system to regulate the floating voltages across the capacitors. This task is more difficult to achieve when the machine operates with relatively large stator currents and at low rotational speed since, at this operating point, large voltage fluctuations may be produced in the capacitors. Therefore, in the so-called "low-frequency mode" (LFM), mitigation is required to reduce the capacitor voltage fluctuations using quantities such as additional circulating currents and common-mode voltages (hereafter called "mitigating variables"). Conversely, when the mitigation is no longer required, the "high-frequency mode" (HFM) is usually enabled [10], [11], [15], [20].

Several control systems have been proposed for both operating modes [6], [12], [14], [16]. However, in those papers only the electrical frequency ω_e is utilized to define the operating mode of the converter, neglecting the influence of any additional operating conditions (such as the torque for example). If ω_e is used alone to define the operating point, the mitigation variables may be applied even when they are not required, degrading the converter efficiency and performance. Another drawback with the control systems reported in the literature [6], [12], [14], [16] is that the mitigating currents typically increase with the machine frequency, which could lead to oversizing of some converter components. Moreover, it is important to notice that in most of the control systems discussed previously, the mitigation variables are designed to drive the capacitor voltage fluctuations to zero. This is not strictly necessary, since restricting the voltage fluctuations inside a suitable band, e.g., 5%–10% of the nominal voltage, is enough to ensure appropriate performance [10], [11].

In a recent paper, a control algorithm to partially mitigate the capacitor voltage oscillations [17] was proposed. Although a reduction of the required circulating currents was achieved with the method reported, only simulation results were used to validate the proposed methodology for drive applications. The experimental results provided in [17] were obtained using a passive *RL* load, considering operation only in the low-speed mode. Moreover the mitigation signals are calculated offline and lack the necessary adaptation capability to compensate for possible changes in the operating point of the drive [16].

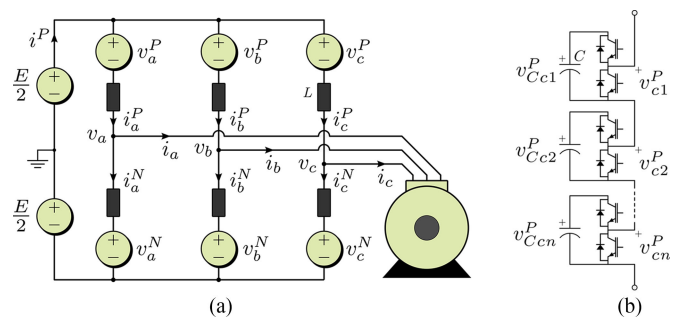

Fig. 1. MMC-based drive. (a) Converter topology. (b) Cluster.

In this paper, a new control strategy to regulate the voltage fluctuations is proposed. This algorithm implements a fast-dynamic closed-loop vector control strategy that regulates the measured capacitor voltage fluctuations inside a predefined threshold. The stator electrical frequency ω_e is not the only criterion used to define the converter operating mode. Moreover, in contrast to previous works, seamless operation, without a large transition zone, is achieved using the proposed control methodology. Elimination of the transition zone is a very important contribution of this paper since the largest circulating currents are typically reached during this transition [6]. This paper also proposes to combine vector control of the voltage fluctuations with flux weakened operation of the cage machine. Moreover, because closed-loop control is proposed, variations and perturbations in the system, e.g., changes in the common mode voltage waveform, mechanical load changes, etc., can be compensated using the proposed control methodology.

The remainder of this paper is organized as follows. Modeling of the MMC-based drive is briefly discussed in Section II. An analysis of the capacitor voltage fluctuations is presented in Section III, while the proposed control systems and the implementation of the converter operating modes are discussed in Section IV. Experimental results obtained from an 18-cell MMC-based drive prototype, operating over the full speed range, are discussed in Section V. Finally, Section VI presents the conclusions of this paper.

II. Modeling of the MMC

Recently, a new model for the MMC has been reported in [14], [16]. In these papers, a $\Sigma\Delta\alpha\beta 0$-transformation is used to represent the MMC currents and total cluster voltages (the sum of the capacitor voltages in a cluster) in a coordinate system that simplifies decoupled control of the MMC. A brief review of this modeling approach is given here to provide the required context for the further developments.

The dynamics of the MMC-based drive are obtained from Fig. 1 as follows [14]:

$$L\frac{d}{dt}\overbrace{\begin{bmatrix} i_a^P & i_b^P & i_c^P \\ i_a^N & i_b^N & i_c^N \end{bmatrix}}^{\doteq \mathbf{I}_{abc}^{PN}} = -\overbrace{\begin{bmatrix} v_a^P & v_b^P & v_c^P \\ v_a^N & v_b^N & v_c^N \end{bmatrix}}^{\doteq \mathbf{V}_{abc}^{PN}} - \frac{E}{2}\begin{bmatrix} 1 & 1 & 1 \\ 1 & 1 & 1 \end{bmatrix} + \begin{bmatrix} -v_a & -v_b & -v_c \\ v_a & v_b & v_c \end{bmatrix} \tag{1}$$

$$C\bar{v}_C\frac{d}{dt}\underbrace{\begin{bmatrix} v_{Ca}^P & v_{Cb}^P & v_{Cc}^P \\ v_{Ca}^N & v_{Cb}^N & v_{Cc}^N \end{bmatrix}}_{\doteq \mathbf{V}_{Cabc}^{PN}} \approx \underbrace{\begin{bmatrix} p_a^P & p_b^P & p_c^P \\ p_a^N & p_b^N & p_c^N \end{bmatrix}}_{\doteq \mathbf{P}_{abc}^{PN}} \tag{2}$$

where $\bar{v}_C$ is the algebraic mean value of the voltage in all capacitors of the MMC, $p_a^P = i_a^P v_a^P$, $p_b^P = i_b^P v_b^P$, etc., are the cluster power fluctuations and $v_{Ca}^P = v_{Ca1}^P + v_{Ca2}^P + ... + v_{Can}^P$, $v_{Ca}^N = v_{Ca1}^N + v_{Ca2}^N + ... + v_{Can}^N$, etc., are the total cluster voltages. Equation (1) is obtained by applying Kirchhoff's voltage law to the converter depicted in Fig. 1. On the other hand, (2) denotes the energy balance in the MMC clusters, assuming that the total cluster voltages are maintained around the reference voltage, with relatively small ripple.

As discussed before, to achieve decoupled control of the converter currents and voltages, the $\Sigma\Delta\alpha\beta 0$-transformation is utilized. This transformation is given by

$$\mathbf{X}_{\alpha\beta 0}^{\Sigma\Delta} \doteq \mathbf{C}^{\Sigma\Delta} \cdot \mathbf{X}_{abc}^{PN} \cdot \mathbf{C}_{\alpha\beta 0}^{\mathsf{T}} \tag{3}$$

where $\mathbf{X}_{abc}^{PN}$ represents the matrix to be transformed (e.g., $\mathbf{I}_{abc}^{PN}$ or $\mathbf{V}_{abc}^{PN}$) and the matrices $\mathbf{C}^{\Sigma\Delta}$ and $\mathbf{C}_{\alpha\beta 0}^{\mathsf{T}}$ are

$$\mathbf{C}^{\Sigma\Delta} = \begin{bmatrix} \frac{1}{2} & \frac{1}{2} \\ 1 & -1 \end{bmatrix}, \quad \mathbf{C}_{\alpha\beta 0}^{\mathsf{T}} = \begin{bmatrix} \frac{2}{3} & \frac{-1}{3} & \frac{-1}{3} \\ 0 & \frac{1}{\sqrt{3}} & \frac{-1}{\sqrt{3}} \\ \frac{1}{3} & \frac{1}{3} & \frac{1}{3} \end{bmatrix}^{\mathsf{T}}. \tag{4}$$

Therefore, applying (3) to (1) and (2) yields

$$L\frac{d}{dt}\overbrace{\begin{bmatrix} i_\alpha^\Sigma & i_\beta^\Sigma & \frac{1}{3}i^P \\ i_\alpha & i_\beta & 0 \end{bmatrix}}^{\doteq \mathbf{I}_{\alpha\beta 0}^{\Sigma\Delta}} = -\overbrace{\begin{bmatrix} v_\alpha^\Sigma & v_\beta^\Sigma & v_0^\Sigma \\ v_\alpha^\Delta & v_\beta^\Delta & v_0^\Delta \end{bmatrix}}^{\doteq \mathbf{V}_{\alpha\beta 0}^{\Sigma\Delta}} - 2\begin{bmatrix} 0 & 0 & -\frac{1}{4}E \\ v_\alpha & v_\beta & v_0 \end{bmatrix} \tag{5}$$

$$C\bar{v}_C\frac{d}{dt}\underbrace{\begin{bmatrix} v_{C\alpha}^\Sigma & v_{C\beta}^\Sigma & v_{C0}^\Sigma \\ v_{C\alpha}^\Delta & v_{C\beta}^\Delta & v_{C0}^\Delta \end{bmatrix}}_{\doteq \mathbf{V}_{C\alpha\beta 0}^{\Sigma\Delta}} \approx \underbrace{\begin{bmatrix} p_\alpha^\Sigma & p_\beta^\Sigma & p_0^\Sigma \\ p_\alpha^\Delta & p_\beta^\Delta & p_0^\Delta \end{bmatrix}}_{\doteq \mathbf{P}_{\alpha\beta 0}^{\Sigma\Delta}} \tag{6}$$

where the machine currents (i_α and i_β) and voltages (v_α, v_β, and v_0) are expressed in $\alpha\beta 0$-coordinates, i_α^Σ and i_β^Σ are the circulating currents and i^P is the dc port current. Based on (5), each current in $\mathbf{I}_{\alpha\beta 0}^{\Sigma\Delta}$ can be controlled by manipulating only one component of the matrix $\mathbf{V}_{\alpha\beta 0}^{\Sigma\Delta}$, which is composed of the output cluster voltages of the MMC in the $\Sigma\Delta\alpha\beta 0$-coordinate system. Moreover, the machine common-mode voltage v_0 is defined by modifying v_0^Δ [$v_0^\Delta = -2v_0$, see (5)]. As discussed in Section III-A, decoupled control of the circulating currents i_α^Σ, i_β^Σ and the common-mode voltage v_0, is useful since these variables are utilized to mitigate the otherwise large fluctuations of the capacitor voltages in the LFM.

The vector representation of (6) is more appropriate for the implementation of high-dynamic performance vector control strategies. Defining the power flows and the total cluster voltages as vectors (e.g., $\mathbf{p}_{\alpha\beta}^\Sigma = p_\alpha^\Sigma + jp_\beta^\Sigma$, $\mathbf{v}_{C\alpha\beta}^\Sigma = v_{C\alpha}^\Sigma + jv_{C\beta}^\Sigma$, etc.), the vector model of (6) is obtained as (see [16])

$$C\bar{v}_C\frac{d\mathbf{v}_{C\alpha\beta}^\Sigma}{dt} \approx \mathbf{p}_{\alpha\beta}^\Sigma \approx \frac{1}{2}E\mathbf{i}_{\alpha\beta}^\Sigma - \frac{1}{4}(\mathbf{i}_{\alpha\beta}\mathbf{v}_{\alpha\beta})^c - \frac{1}{2}v_0\mathbf{i}_{\alpha\beta} \tag{7a}$$

$$C\bar{v}_C\frac{d\mathbf{v}_{C\alpha\beta}^\Delta}{dt} \approx \mathbf{p}_{\alpha\beta}^\Delta \approx \frac{1}{2}E\mathbf{i}_{\alpha\beta} - \frac{2}{3}i^P\mathbf{v}_{\alpha\beta} - (\mathbf{v}_{\alpha\beta}\mathbf{i}_{\alpha\beta}^\Sigma)^c - 2v_0\mathbf{i}_{\alpha\beta}^\Sigma \tag{7b}$$

$$C\bar{v}_C\frac{dv_{C0}^\Sigma}{dt} \approx p_0^\Sigma \approx \frac{1}{6}Ei^P - \frac{1}{4}\Re\left[\mathbf{v}_{\alpha\beta}\left(\mathbf{i}_{\alpha\beta}\right)^c\right] \tag{7c}$$

$$C\bar{v}_C\frac{dv_{C0}^\Delta}{dt} \approx p_0^\Delta \approx -\Re\left[\mathbf{v}_{\alpha\beta}\left(\mathbf{i}_{\alpha\beta}^\Sigma\right)^c\right] - \frac{2}{3}i^P v_0 \tag{7d}$$

where " ^{c} " stands for the complex conjugation operator.

III. Analysis of the MMC-Based Drive

A. Voltage Fluctuations in the Converter Capacitors

If $\mathbf{i}_{\alpha\beta}^\Sigma$ and v_0 are zero (i.e., no mitigation variables are applied), the steady-state total cluster voltages in the $\Sigma\Delta\alpha\beta 0$-domain can be obtained from (7a)–(7d) as

$$\mathbf{v}_{C\alpha\beta}^\Delta \approx \frac{1}{j\omega_e C\bar{v}_C}\left(\frac{1}{2}E\mathbf{i}_{\alpha\beta} - \frac{2}{3}i^P\mathbf{v}_{\alpha\beta}\right) \tag{8a}$$

$$\mathbf{v}_{C\alpha\beta}^\Sigma \approx \frac{-1}{j8\omega_e C\bar{v}_C}\left(\mathbf{i}_{\alpha\beta}\mathbf{v}_{\alpha\beta}\right)^c \tag{8b}$$

$$v_{C0}^\Sigma \approx n\bar{v}_C, \quad v_{C0}^\Delta \approx 0. \tag{8c}$$

Based on the inverse $\Sigma\Delta\alpha\beta 0$-transformation, the total capacitor voltages in $PNabc$-coordinates can be expressed using the vector voltages previously defined. For example, it can be demonstrated that the voltages v_{Ca}^P and v_{Ca}^N are given as follows:

$$v_{Ca}^P = \frac{1}{2}\Re\left[\mathbf{v}_{C\alpha\beta}^\Delta\right] + \Re\left[\mathbf{v}_{C\alpha\beta}^\Sigma\right] + \frac{1}{2}v_{C0}^\Delta + v_{C0}^\Sigma \tag{9a}$$

$$v_{Ca}^N = -\frac{1}{2}\Re\left[\mathbf{v}_{C\alpha\beta}^\Delta\right] + \Re\left[\mathbf{v}_{C\alpha\beta}^\Sigma\right] - \frac{1}{2}v_{C0}^\Delta + v_{C0}^\Sigma. \tag{9b}$$

Considering (8a)–(8c) and (9a)–(9b), it is concluded that the total cluster voltages are mainly composed of a mean value given by v_{C0}^Σ, a fundamental fluctuation of frequency ω_e defined by $\mathbf{v}_{C\alpha\beta}^\Delta$, and a double frequency term given by $\mathbf{v}_{C\alpha\beta}^\Sigma$. Therefore, considering the worst case situation, the maximum amplitude of the oscillating component of the total cluster voltages $|\tilde{v}_{Cx}^X|$ can be related with the vector voltages $\mathbf{v}_{C\alpha\beta}^\Delta$ and $\mathbf{v}_{C\alpha\beta}^\Sigma$ as follows:

$$|\tilde{v}_{Cx}^X| = \frac{1}{2}|\mathbf{v}_{C\alpha\beta}^\Delta| + |\mathbf{v}_{C\alpha\beta}^\Sigma| \tag{10}$$

where the symbol "~" denotes the oscillating (ac) component of a variable $x \in \{a, b, c\}$ and $X \in \{P, N\}$.

As discussed in [10], [11], the voltage fluctuation defined in (10) can exceed an acceptable amplitude depending on the converter operating point. Notice that the vector $\mathbf{v}^{\Delta}_{C\alpha\beta}$ contributes the most to the large fluctuations at machine start-up, mainly if high currents are required [16].

As depicted in (8a), in steady state, the voltage $\mathbf{v}^{\Delta}_{C\alpha\beta}$ has an oscillating component of frequency ω_e. Considering the advantages of vector control systems for the regulation of power converters and electrical machines (see [16], [21]), in this paper the voltage fluctuations of (7b) are referred to a synchronous dq-frame rotating at ω_e, where ω_e is the frequency of the signals applied to the stator of the induction machine. Therefore, in this paper, a complex vector $\mathbf{x}_{\alpha\beta} = x_\alpha + jx_\beta$, expressed in the $\alpha\beta$-coordinate system, is referred into the dq-coordinate system applying the following complex transformation:

$$\mathbf{x}_{dq} = \mathbf{x}_{\alpha\beta} e^{-j\theta_e} \tag{11}$$

where $\theta_e = \int \omega_e dt$.

For drive applications, both θ_e and ω_e are defined by the machine control system. Therefore, applying (11) to (7b) and reordering yields

$$C\bar{v}_C \frac{d\mathbf{v}^{\Delta}_{Cdq}}{dt} \approx \underbrace{\frac{1}{2}E\mathbf{i}_{dq} - \frac{2}{3}i^P\mathbf{v}_{dq}}_{\doteq \mathbf{p}_{\omega_e}} - \underbrace{jC\bar{v}_C\omega_e\mathbf{v}^{\Delta}_{Cdq}}_{\doteq \mathbf{p}_m} - \underbrace{2v_0\mathbf{i}^{\Sigma}_{dq}}_{\doteq \mathbf{p}_c} \tag{12}$$

where the term $(\mathbf{v}_{\alpha\beta}\mathbf{i}^{\Sigma}_{\alpha\beta})^c$ in (7b) has been neglected, since it produces small fluctuations in the capacitor voltages if the frequency of $\mathbf{i}^{\Sigma}_{\alpha\beta}$ is high in comparison with the frequency ω_e of $\mathbf{v}_{\alpha\beta}$. In (12), the power fluctuation $\mathbf{p}_{\omega_e}$ can produce large fluctuations in $\mathbf{v}^{\Delta}_{Cdq}$ depending on the drive operating point, the vector $\mathbf{p}_m$ is a coupling term and $\mathbf{p}_c$ is a degree of freedom. For example, the common-mode voltage and the circulating currents can be in-phase to manipulate the power $\mathbf{p}_c$ in order to regulate $\mathbf{v}^{\Delta}_{Cdq}$ as required to eliminate $\mathbf{p}_{\omega_e}$ and $\mathbf{p}_m$ during the LFM. To perform this task, high-frequency components are utilized in $\mathbf{p}_c = 2v_0\mathbf{i}^{\Sigma}_{dq}$ to avoid the generation of any low-frequency power pulsations in (7a)–(7d). In steady state and considering ideal conditions, the required set-point values of $\tilde{\mathbf{i}}^{\Sigma}_{dq}$ and $\tilde{v}_0$, are defined as

$$\tilde{\mathbf{i}}^{\Sigma *}_{dq} = \frac{1}{2V_0}\left(\mathbf{p}_{\omega_e} - \mathbf{p}_m\right) f(t) \tag{13}$$

$$\tilde{v}^*_0 = V_0 \operatorname{sign}\left[f(t)\right] \tag{14}$$

where " * " stands for the desired value of a variable and V_0 is the amplitude of the common-mode voltage. Consequently, the resultant power $\mathbf{p}_c$ is

$$\mathbf{p}_c = \left(\mathbf{p}_{\omega_e} - \mathbf{p}_m\right)|f(t)|. \tag{15}$$

Hence, $\mathbf{p}_{\omega_e}$ and $\mathbf{p}_m$ are eliminated from (12) if $f(t)$ is a high-frequency signal compared to ω_e during LFM, such that the mean value of $|f(t)| = 1$ (considering one period of $f(t)$). In the experimental results of Section V, a function $f(t) = 1.57\sin(100\pi t)$ is utilized. Additional discussions regarding the function $f(t)$ and other options to define the common-mode voltage are presented in [10], [11], [15].

B. Influence of the Vector $\mathbf{v}^{\Delta}_{Cdq}$ on the Mitigating Variables

Conventionally, the set-point value of $\mathbf{v}^{\Delta}_{Cdq}$ is assigned to zero in the LFM to eliminate any fundamental voltage fluctuation in the MMC capacitors. This procedure generates high circulating currents as ω_e increases, because the available cluster voltage has to be used to synthesize the machine voltage, reducing the value of V_0 [see (13)]. However, in this paper a methodology to reduce the circulating currents by using a specific nonzero set-point value for $\mathbf{v}^{\Delta}_{Cdq}$ is proposed.

From (13), it can be concluded that the magnitudes of the circulating currents are minimized if the vectors $\mathbf{p}_{\omega_e}$ and $\mathbf{p}_m$ have the same phase shift. This condition is fulfilled if $\mathbf{p}_m$ is defined in terms of $\mathbf{p}_{\omega_e}$ as

$$\mathbf{p}^*_m = jC\bar{v}^*_C\omega_e\mathbf{v}^{\Delta *}_{Cdq} = C\bar{v}^*_C|\omega_e||\mathbf{v}^{\Delta *}_{Cdq}|\hat{\mathbf{p}}_{\omega_e} \tag{16}$$

where $\hat{\mathbf{p}}_{\omega_e} = \frac{\mathbf{p}_{\omega_e}}{|\mathbf{p}_{\omega_e}|}$ is a unit vector in-phase with $\mathbf{p}_{\omega_e}$. Thus, assuming $\mathbf{p}^*_m = \mathbf{p}_m$ and inserting (16) into (13) yields

$$\tilde{\mathbf{i}}^{\Sigma *}_{dq} = \frac{1}{2V_0}\left(|\mathbf{p}_{\omega_e}| - C\bar{v}^*_C|\omega_e||\mathbf{v}^{\Delta *}_{Cdq}|\right)\hat{\mathbf{p}}_{\omega_e} f(t). \tag{17}$$

Based on (17), it can be concluded that the amplitude of the resultant circulating currents will be less or equal (at $\omega_e \approx 0$) to that obtained if $\mathbf{v}^{\Delta *}_{Cdq}$ and consequently $\mathbf{p}^*_m$ are set to zero during the LFM [see (13)]. This improvement represents an important contribution to the performance and efficiency of MMC-based drives. However, $|\mathbf{v}^{\Delta *}_{Cdq}|$ must be related to the maximum fluctuations of the total cluster voltages to maintain their amplitudes inside an acceptable threshold. Using (10) and considering $|\mathbf{v}^{\Delta}_{Cdq}| = |\mathbf{v}^{\Delta}_{C\alpha\beta}|$, $|\mathbf{v}^{\Delta *}_{Cdq}|$ is expressed as follows:

$$|\mathbf{v}^{\Delta *}_{Cdq}| = 2\left(|\tilde{v}^{X *}_{Cx}| - |\mathbf{v}^{\Sigma}_{C\alpha\beta}|\right). \tag{18}$$

Finally, from (18) and (16), $\mathbf{v}^{\Delta *}_{Cdq}$ is calculated as

$$\mathbf{v}^{\Delta *}_{Cdq} = -j2\operatorname{sign}[\omega_e]\left(|\tilde{v}^{X *}_{Cx}| - |\mathbf{v}^{\Sigma}_{C\alpha\beta}|\right)\hat{\mathbf{p}}_{\omega_e}. \tag{19}$$

Accordingly, the set-point value of $\tilde{\mathbf{i}}^{\Sigma}_{dq}$ can be automatically defined by an MMC control system that regulates $\mathbf{v}^{\Delta}_{Cdq}$ to follow $\mathbf{v}^{\Delta *}_{Cdq}$ given by (19). Furthermore, the circulating currents of (17) could be used as a feed-forward term to improve the dynamic response if required. A control system implementing this algorithm is presented in Section IV. Moreover, any nonlinearity or change in the drive parameters is compensated by the closed-loop control system, while the fluctuations of the total cluster voltages are well regulated and are inside the voltage threshold defined by $|\tilde{v}^{X *}_{Cx}|$. This is illustrated in Fig. 2, where an example total cluster voltage is shown, considering that a nonzero $|\tilde{v}^{X *}_{Cx}|$ is regulated by the control system (see the black line). The expected voltage fluctuation in the cluster when no mitigating variables are used is also shown in Fig. 2, illustrating clearly the need for mitigation.

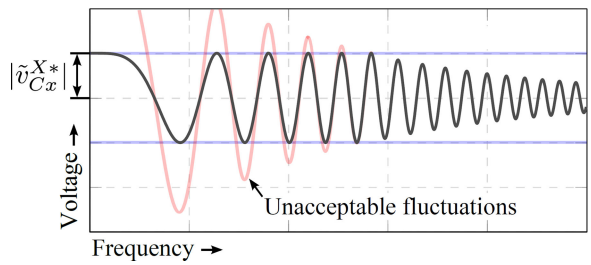

Fig. 2. Expected behavior of the total cluster voltage using the proposed strategy (black) and without mitigating variables (red).

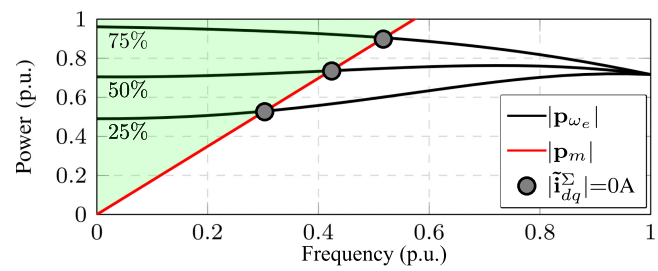

Fig. 4. $|\mathbf{p}_{\omega_e}|$ and $|\mathbf{p}_m|$ as a function of the MMC operating point.

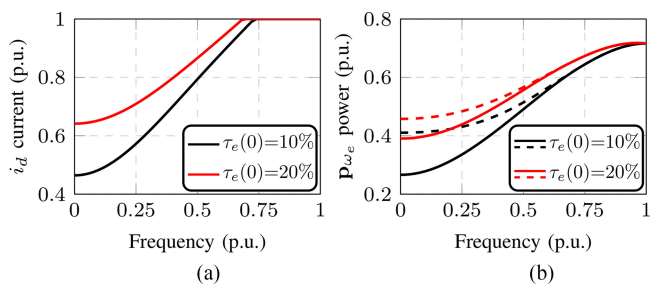

Fig. 3. MMC variables as a function of the electrical frequency and torque loads. (a) Optimal d-axis current. (b) Amplitude of the vector $\mathbf{p}_{\omega_e}$ (solid-lines: optimal $|\mathbf{p}_{\omega_e}|$, dashed-lines: nominal $|\mathbf{p}_{\omega_e}|$).

C. Flux-Weakening Operation of the MMC-Based Drive

Another option to reduce the amplitude of the circulating currents is to minimize $|\mathbf{p}_{\omega_e}|$ [see (17)]. Notice that $\mathbf{p}_{\omega_e}$ can be represented as a function of E and $\mathbf{i}_{dq}$ (i.e., $\mathbf{p}_{\omega_e} = \mathbf{p}_{\omega_e}(E, i_d, i_q)$) using the machine model (including saturation effects) and the power balance between the input and output converter ports. Therefore, if the dc port voltage is considered constant and the torque current i_q is defined by the speed control system, it is possible to define the following constrained optimization problem to minimize $|\mathbf{p}_{\omega_e}|$ varying the flux current i_d

$$\min_{i_d} |\mathbf{p}_{\omega_e}(E, i_d, i_q)| \text{ s.t. } \begin{cases} p\frac{L_m^2}{L_r} i_d i_q = \tau_e(\omega_e) \\ \sqrt{i_d^2 + i_q^2} < i_{\max} \end{cases} \tag{20}$$

where p is the number of pole-pairs, L_m and L_r are the magnetizing and rotor inductances, respectively (which are not constant due to flux weakening) and $i_{\max}$ is the maximum machine current. Two constraints have been defined in (20) to obtain the required electrical torque in the machine, $\tau_e(\omega_e)$, while keeping the stator current magnitude below $i_{\max}$.

Fig. 3(a) shows the optimal values of i_d obtained when the parameters of the MMC-based drive utilized in this paper are used to solve the optimization problem of (20), showing that the magnitude of $\mathbf{p}_{\omega_e}$ is reduced (particularly for low ω_e values) when flux-weakening operation is applied. To obtain this figure, the electrical torque characteristic was defined as

$$\tau_e(\omega_{e(\text{p.u.})}) = \tau_e(0) + [1 - \tau_e(0)]\, \omega_{e(\text{p.u.})}^2 \tag{21}$$

where $\omega_{e(\text{p.u.})} \leq 1$ is the per unit machine frequency and $\tau_e(0) < 1$ is the initial torque load.

A comparison of the magnitude of $\mathbf{p}_{\omega_e}$ when the optimal (solid-lines) and nominal (dashed-lines) values of i_d are used is depicted in Fig. 3(b). As shown in this graphic, the flux-weakening operation at the machine start-up is an attractive option for mechanical loads requiring low torques at low rotational speeds [e.g., see the variation in $\mathbf{p}_{\omega_e}$ for $\tau_e(0) = 10\%$ in Fig. 3(b)], such as blowers, fans, pumps, and wind energy conversion systems. A discussion of some issues related to the implementation of vector control strategies for cage induction machines in flux-weakening operation, e.g., the variation of the machine inductances due to saturation effects, are presented in [21].

D. Transition Between Operating Modes

The transition between the LFMs and HFMs when the proposed strategies are used can be explained using Fig. 4. In the figure, the magnitude of $\mathbf{p}_{\omega_e}$ and $\mathbf{p}_m$ is depicted when a drive is feeding a machine such as that used in Section V (see experimental results) for three different values of $\tau_e(0)$ [see (21)]. As the figure shows, the LFM has to be enabled when $|\mathbf{p}_{\omega_e}| > |\mathbf{p}_m|$ (see the green area of Fig. 4) since the power $\mathbf{p}_c$ is required to regulate the voltage fluctuations of the total cluster voltages within the threshold defined by $|\tilde{v}_{Cx}^{X*}|$ [see (12)]. However, when $|\mathbf{p}_{\omega_e}| \leq |\mathbf{p}_m|$ the mitigating variables are no longer required because the tendency of the total capacitor voltage fluctuation is to decrease as ω_e increases [see (12) and (8a)] and the HFM is then enabled. During the HFM, $\mathbf{p}_c = 2v_0\tilde{\mathbf{i}}_{dq}^{\Sigma}$ is used only to ensure a zero-mean value in the voltages $v_{C\alpha}^{\Delta}$ and $v_{C\beta}^{\Delta}$. Therefore, v_0 can be defined to reduce the peak value of the output cluster voltage by injecting a third harmonic voltage, while the circulating currents have a component in-phase with v_0 (further details are in [14], [16]). Finally, notice that the operating region of the LFM can be manipulated by varying the slope of $|\mathbf{p}_m|$ (e.g., by choosing $|\tilde{v}_{Cx}^{X*}|$ or C) and it is also affected by the machine torque, demonstrating the importance to consider more information other than only the frequency ω_e in the selection of the converter mode.

IV. Proposed Control Systems

In this section, the control systems required to operate the MMC-based drive are presented and discussed. They are based on a cascaded structure, where the outer control loops regulate the $\Sigma\Delta\alpha\beta 0$ capacitor voltages defined in (6). Meanwhile, the

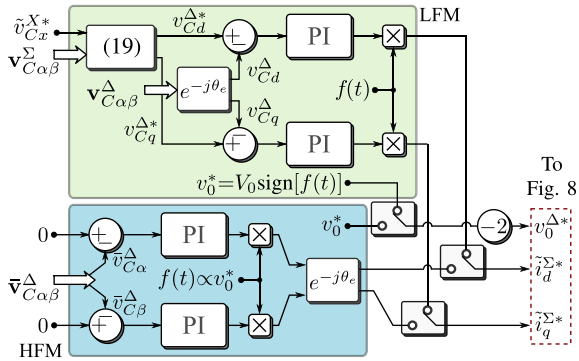

Fig. 5. Control of the vector $\mathbf{v}^{\Delta}_{C\alpha\beta}$.

inner controllers regulate the cluster currents by manipulating the output cluster voltages $\mathbf{V}^{PN}_{abc}$ [see (5)].

A. Vector Control of $\mathbf{v}^{\Delta}_{C\alpha\beta}$

The control system utilized to regulate the vector $\mathbf{v}^{\Delta}_{C\alpha\beta}$ is shown in Fig. 5 (further details are discussed in [16]). In both operating modes (LFM and HFM), $\mathbf{v}^{\Delta}_{C\alpha\beta}$ is regulated by manipulating the power fluctuation $\mathbf{p}_c = 2\tilde{\mathbf{i}}^{\Sigma}_{dq}\tilde{v}_0$.

During the LFM (see the green area of Fig. 5), $\mathbf{v}^{\Delta}_{Cdq}$ is regulated with zero steady-state error using two proportional-integral (PI) controllers, whose outputs are multiplied by the function $f(t)$ to create the desired ac component of the circulating currents in dq-coordinates. One of the most important contributions and differences of this paper when compared with the most recent approaches reported in the literature [16] is that the setpoint value of the voltage vector $\mathbf{v}^{\Delta}_{Cdq}$, $\mathbf{v}^{\Delta *}_{Cdq} = v^{\Delta *}_{Cd} + jv^{\Delta *}_{Cq}$ is a nonzero vector. Moreover using the value of $\mathbf{v}^{\Delta *}_{Cdq}$ calculated from (19), it is ensured that the fluctuations of the total cluster voltages are maintained inside the band defined by $\tilde{v}^{X*}_{Cx}$ (see Section III-B). Additionally, a reduction in the magnitude of the circulating currents, as the machine frequency increases, is also achieved. It is not possible to obtain this reduction when a null vector $\mathbf{v}^{\Delta *}_{Cdq}$ is applied to the control system.

The control system depicted in the light-blue area of Fig. 5 is used to regulate $\mathbf{v}^{\Delta}_{C\alpha\beta}$ in the HFM. This is achieved by regulating its average value, $\bar{\mathbf{v}}^{\Delta}_{C\alpha\beta}$ (which is obtained by applying filters to $\mathbf{v}^{\Delta}_{C\alpha\beta}$) to zero. A dq-synchronous frame transformation is then used at the output of the control system to generate the desired values of the ac circulating currents.

Notice that $v_0^* = -\frac{1}{2}v_0^{\Delta}$ [see (5)] and $f(t)$ have different design methodologies in each mode [14], [16]. For the LFM, v_0^* and $f(t)$ are defined as high-frequency signals with the magnitude of v_0^* as high as possible to reduce the circulating currents [see (13)]. Meanwhile, in the HFM they can be configured to inject third harmonic components in the modulation stage, maximizing the modulation index [14]. The tuning of the PI parameters is robust against variations in the induction machine load, because the manipulated power $\mathbf{p}_c$ is not affected much by the loading conditions [see (12)]. This is further corroborated by the experimental results discussed in Section V-B.

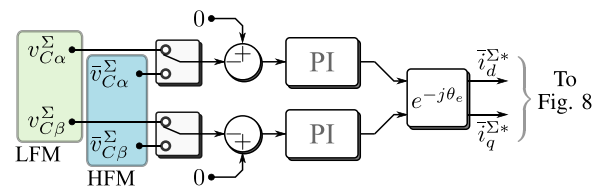

Fig. 6. Control of the vector $\mathbf{v}^{\Sigma}_{C\alpha\beta}$.

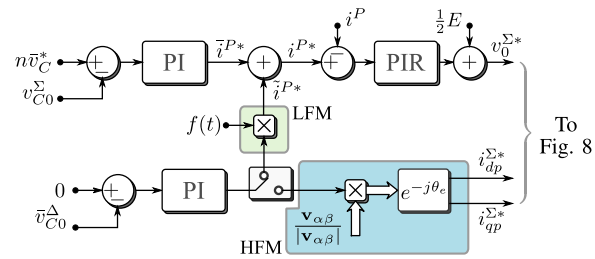

Fig. 7. Control of the voltages v^{Σ}_{C0} and v^{Δ}_{C0}.

An additional difference to recent approaches reported in the literature [14], [16], [22] is that the proposed control system uses software-implemented switches to achieve a fast transition between the operating modes, avoiding the use of weighting factors to change the control system from the LFM to the HFMs. In this paper, a seamless transition is possible because the circulating currents become null at the end of the LFM (see Fig. 4). This is certainly an advantage over previous works (see [14], [16], [22]), where a transition zone with relatively large circulating currents is typically produced, degrading the converter efficiency.

B. Control of the Vector $\mathbf{v}^{\Sigma}_{C\alpha\beta}$

The regulation of $\mathbf{v}^{\Sigma}_{C\alpha\beta}$ is realized by adding a dc component in the circulating currents to create a manipulable power with the dc port voltage E [see (7a)]. As shown in the green area of Fig. 6, two PI controllers are required to generate this dc circulating current in the LFM. In this mode, the vector $\mathbf{v}^{\Sigma}_{C\alpha\beta}$ is directly regulated. However, when the switches enable the HFM (see the light-blue area of Fig. 6) only the low-frequency components of $\mathbf{v}^{\Sigma}_{C\alpha\beta}$ ($\bar{\mathbf{v}}^{\Sigma}_{C\alpha\beta}$) are regulated avoiding the presence of circulating currents in steady state.

C. Control of the Voltages v^{Σ}_{C0} and v^{Δ}_{C0}

The voltage v^{Σ}_{C0} is regulated by using a dc component in i^P, as shown at the top of Fig. 7 [see (7c)]. The voltage v^{Δ}_{C0} [see (7d)] can be regulated using: 1) an ac component in i^P which produces a nonzero mean power with the common-mode voltage (i.e., a proportional-integral-resonant controller could be required) or 2) a component of the circulating currents in phase with the machine back electromotive force (EMF) [see (7d)]. Considering that during the LFM the common-mode voltage is high, the first option is used in this mode (see the green area of Fig. 7). The second option is utilized during the HFM considering that the back EMF is high enough in this operating mode (see the light-blue area of Fig. 7).

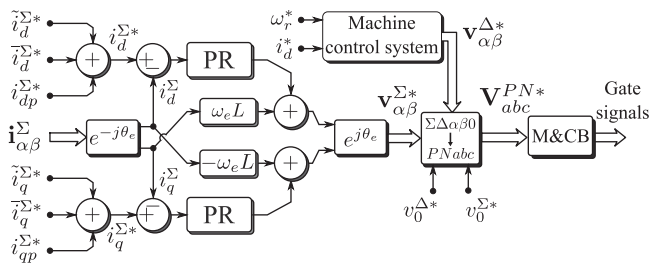

Fig. 8. Circulating current controller and gate signal generation.

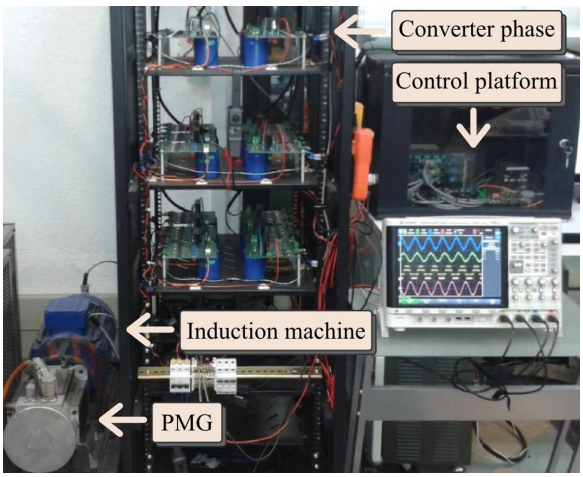

Fig. 9. Photograph of the laboratory experimental system.

TABLE I
SETUP PARAMETERS FOR THE 18 CELLS MMC-DRIVE

Parameter	Symbol	Value	Unit
DC-port voltage	E	450	V
Cluster inductor	L	2,5	mH
Cell capacitor	C	4700	μF
Cell dc voltage	$\bar{v}_C^*$	150	V
Cell count per cluster	n	3	–
Carrier frequency	f_s	5000	Hz

D. Circulating Current Controller and Signal Generator

In the LFM, the dq-circulating currents have the same frequency components as $f(t)$ [see (13)]. Hence, proportional-resonant controllers are appropriate to regulate them, as shown in the control diagram of Fig. 8, which is based on (5). Moreover, the proportional part of the controllers can regulate other components in $\mathbf{i}_{dq}^{\Sigma}$, even in the HFM [22]. At the output of the controller, the inverse dq- and $\Sigma\Delta\alpha\beta 0$-transformations are applied to the desired output cluster voltages in $\Sigma\Delta\alpha\beta 0$-coordinates to obtain $\mathbf{V}_{abc}^{PN*}$. This matrix is then processed by the modulator and cell balancing algorithm (M&CB block in Fig. 8) to determinate the transistor gate signals. In this paper, the cell balancing algorithm presented in [22] and the machine control system discussed in [23] are used.

TABLE II
NOMINAL INDUCTION MACHINE PARAMETERS

Parameter	Value	Unit
Rated output power	7.5	kW
Rated rotating speed	3800	rpm
Line-to-line rms voltage	380	V
Stator rms current	15	A
i_d Magnetizing current	7	A
Pole number	4	–
Rotor resistance	0.724	Ω
Stator resistance	0.660	Ω
Stator inductance	0.141	mH
Rotor inductance	0.141	mH
Mutual inductance	0.138	mH

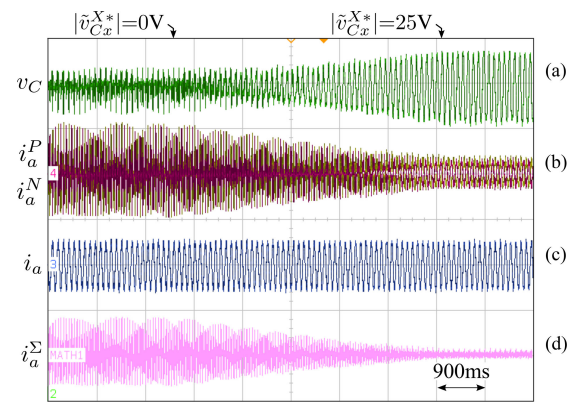

Fig. 10. MMC variables during constant speed operation. From top to bottom: capacitor voltage v_{Ca1}^{P}, cluster currents i_a^P, and i_a^N, machine current i_a, phase circulating current $i_a^{\Sigma} = \frac{1}{2}\left(i_a^P + i_a^N\right)$.

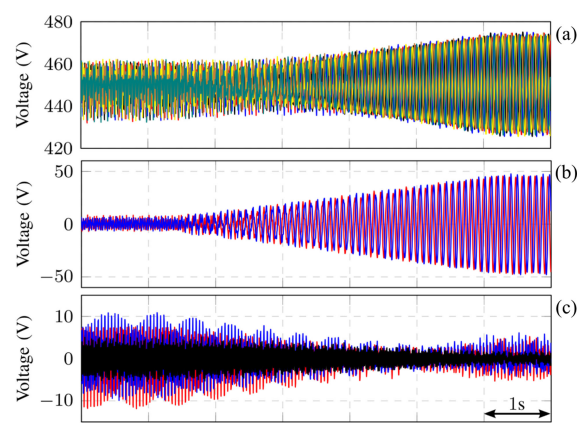

Fig. 11. Total cluster voltages as a function of $|\tilde{v}_{Cx}^{X*}|$ for a constant speed operation. (a) Elements of $\mathbf{V}_{Cabc}^{PN}$, total cluster voltages in $\Sigma\Delta\alpha\beta 0$-coordinates: (b) $v_{C\alpha}^{\Delta}$ and $v_{C\beta}^{\Delta}$, (c) $v_{C\alpha}^{\Sigma}$, $v_{C\beta}^{\Sigma}$, and v_{C0}^{Δ} (black signal).

V. EXPERIMENTAL RESULTS

Experimental results for the proposed control methodology have been obtained using an 18 power cell MMC-based drive. A photograph of the system is presented in Fig. 9 while its parameters are given in Table I. The MMC drives a 7.5-kW

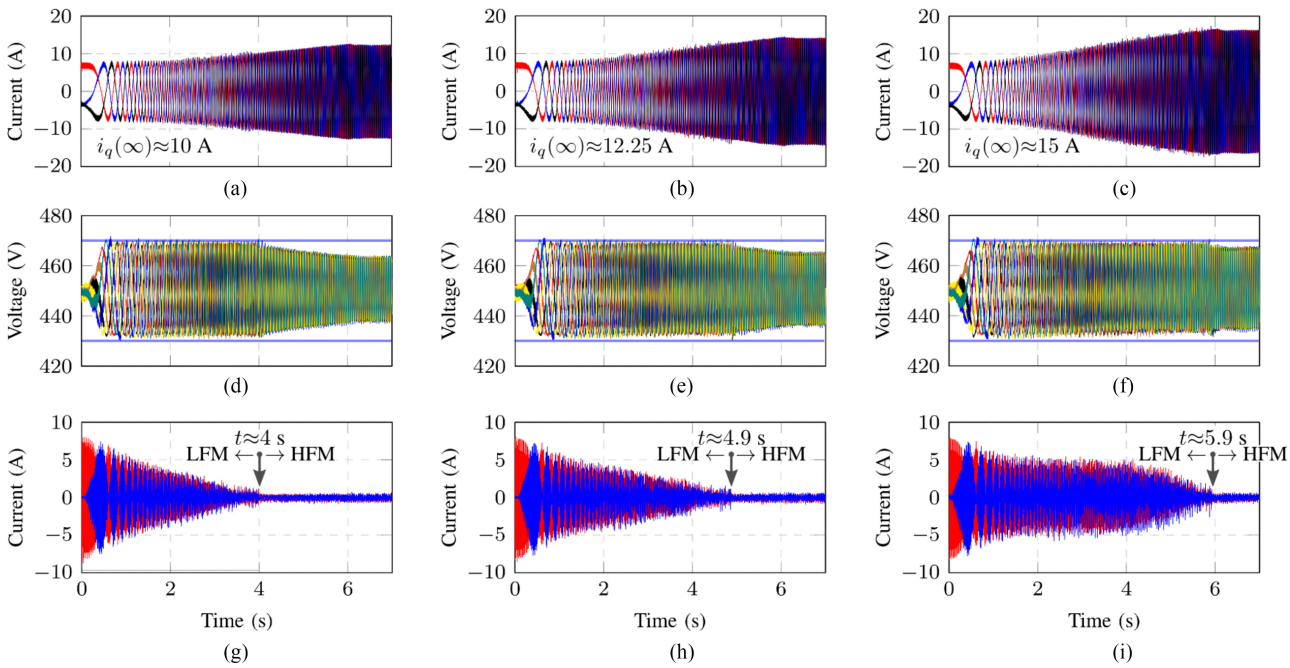

Fig. 12. Dynamic performance of the proposed control strategy for different loading conditions. Left: low-load, center: medium-load, right: maximum-load. (a)–(c) Machine currents i_a, i_b, i_c. (d)–(f) Total cluster voltages v_{Ca}^{P}, v_{Ca}^{N}, etc. (g)–(i) Circulating currents i_α^Σ, i_β^Σ.

vector-controlled induction machine (see Table II) connected to a permanent magnet generator (PMG). A resistor bank has been connected to the PMG output to provide an electrical load. Hall effect transducers are used to measure the dc port voltage, the capacitor voltages, and the cluster currents. A position encoder of 10 000 pulses per revolution is affixed to the induction machine. The system is controlled using a Digital Signal Processor Texas Instrument TMS320C6713 board and two Actel ProAsic3 FPGA boards, equipped with a total of 40 14-bit analogue-digital channels. A phase-shifted pulse width modulation (PWM) algorithm generates the 18 switching signals timed via an FPGA platform. Optical fiber connections transmit the switching signals to the gate drivers of the MOSFET switches (model IRFP4868PbF, nominal ratings of 70 A, 300 V, 32 mΩ on resistance).

A. Performance for Constant Speed Operation

The performance of the control system has been tested considering fixed rotational speed operation at $\omega_r = 600$ r/min (i.e., $\omega_e \approx 2\pi 10$ rad·s^{-1}). For this experimental test the machine is loaded with a constant torque and the control system is regulating a voltage threshold of $|\tilde{v}_{Cx}^{X*}| \approx 0$ V between $t = 0$ s and $t \approx 2.5$ s (see Fig. 10). For $t > 2.5$ s to $t \approx 7.5$ s, the voltage threshold is changed linearly from 0 to 25 V.

As depicted in Fig. 10(a), the cell voltage has negligible fluctuations for $t < 2.5$ s. The corresponding cluster currents are shown in Fig. 10(b). Notice that the peak-to-peak value of these currents is reduced from approximately 40 to 11 A, meanwhile the machine stator current is maintained constant [see Fig. 10(c)]. Finally, the circulating currents are shown in Fig. 10(d). Notice that $i_a^\Sigma \approx 0$A at the end of this test, showing the importance of regulating $|\tilde{v}_{Cx}^{X*}|$ to a nonzero value to reduce the currents of the MMC-based drive during LFM.

Other variables, corresponding to the experimental tests depicted in Fig. 10, have been captured using the DSP control platform. In Fig. 11(a), the total cluster voltages are shown. These are well-regulated with fluctuations that are inside the $|\tilde{v}_{Cx}^{X*}|$ threshold. As discussed before, to perform this regulation, the reference value $\mathbf{v}_{Cdq}^{\Delta *}$ has to be calculated online and used as the input of the control system depicted in Fig. 5. The corresponding amplitudes $v_{C\alpha}^{\Delta}$ and $v_{C\beta}^{\Delta}$ are shown in Fig. 11(b). Their peak-to-peak amplitudes are approximately twice the value of $|\tilde{v}_{Cx}^{X*}|$ [see (18)]. Finally, the consequences of the high circulating currents, produced when $|\tilde{v}_{Cx}^{X*}|$ is low, are illustrated in Fig. 11(c). Notice that the fluctuations in the voltages $v_{C\alpha}^{\Sigma}$, $v_{C\beta}^{\Sigma}$, and v_{C0}^{Δ} become dominant when compared to those obtained in Fig. 11(b). This is due to the terms $E\mathbf{i}_{\alpha\beta}^{\Sigma}$ and $\mathbf{v}_{\alpha\beta}(\mathbf{i}_{\alpha\beta}^{\Sigma})^c$ in (7a) and (7d). When the voltage threshold $|\tilde{v}_{Cx}^{X*}|$ is increased, these oscillations are also reduced.

B. System Performance for Different Loading Conditions

The robustness of the proposed control methodology has been experimentally validated considering different loading conditions. Three experimental tests are shown in Fig. 12. These graphics depict, from top to bottom, the induction machine stator currents, the total cluster voltages, and the circulating currents, corresponding to a ramp speed variation from 0 to 1200 r/min in 6 s. The electrical frequency applied to the stator of the induction machine is shown in Fig. 13.

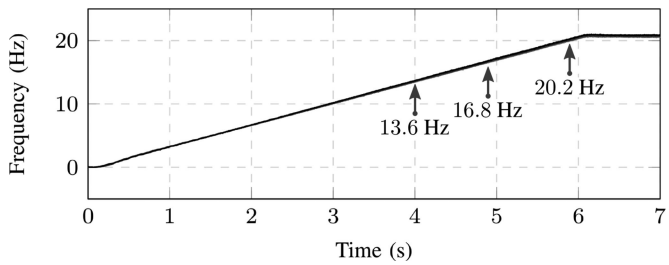

Fig. 13. Electrical machine frequency for different loading conditions. The transition frequencies are indicated in the figure.

To achieve different load conditions, the resistor bank connected to the PMG (see Fig. 9) has been adjusted to produce three different i_q values in steady-state operation, as depicted in Fig. 12(a)–(c). Notice that the peak stator current in Fig. 12(a) is $\approx$ 12 A, increased by 20% for the experimental test shown in Fig. 12(b) and by $\approx$ 35% for the experimental test shown in Fig. 12(c).

The regulation of the total cluster voltage fluctuations during LFM is demonstrated by the results shown in Fig. 12(d)–(f). As expected, the voltages are well regulated and maintained inside the desired voltage band defined by $\tilde{v}_{Cx}^{X*} = 20$ V for the three tests (see the blue lines in the corresponding figures). The circulating currents required for each of the experimental tests are shown in Fig. 12(g)–(i). As discussed in Section III-D, the zone where the LFM is applied is dependent on the loading condition (see Fig. 4), therefore, the transition between LFM and HFM is produced at 4 s when operating at low load, up to 5.9 s for maximum-load operation; however, notice that in all cases the proposed control strategy ensured low circulating currents at the transition point.

The machine frequency for each of the tests is shown in Fig. 13. Although the frequencies are practically overlapped, it can be concluded that the transition frequency is automatically modified by the proposed control system to maintain good regulation of the total cluster voltage fluctuations. This transition frequency varies from 13.6 to 20.2 Hz depending on the machine load [compare Fig. 13 with Fig. 12(g)–(i)]. This experimental result demonstrates the importance of considering more information than that provided by the machine operating frequency alone to change from LFM to HFM. Notice that the use of the machine operating frequency alone to switch from LFM to HFM is the conventional approach reported in previous works (see [14], [16], [17]).

C. Dynamic Performance of the Proposed Control Scheme

The proposed control methodology has been validated in the whole frequency (ω_e) range, including zero crossing. Two different operating conditions are considered: nominal flux and flux-weakening operation. For both cases, the experimental tests are realized using the same speed profile and mechanical load. In all the figures, the operating range of the LFM is depicted using a green background color and the voltage threshold, $|\tilde{v}_{Cx}^{X*}|$, is shown using two blue lines. $|\tilde{v}_{Cx}^{X*}|$ has been defined as $\approx$ three times the peak value of the total cluster voltage fluctuation at full load ($\approx 5\%$ of $\bar{v}_C^*$). With this criterion, the LFM was applied over 33% of the frequency range [see Fig. 4].

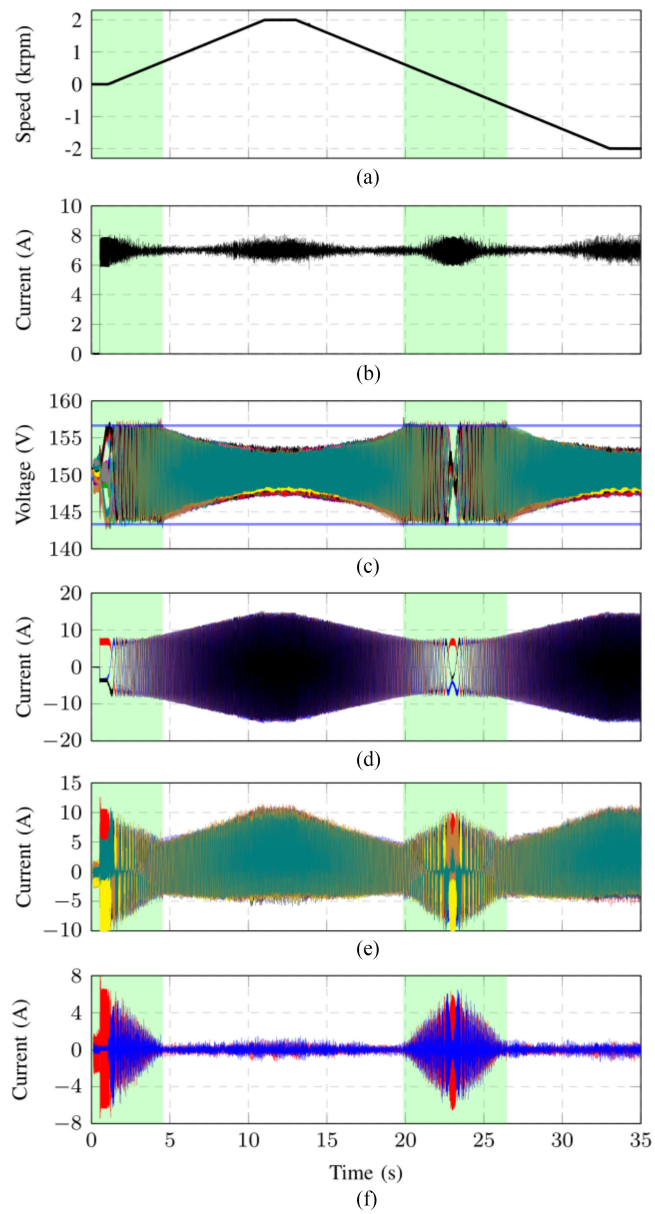

Fig. 14. Experimental results for nominal flux. (a) Machine speed ω_r, (b) d-axis current i_d, (c) capacitor voltages v_{Ca1}^P, v_{Ca2}^P, etc. (the blue lines represent $|\tilde{v}_{Cx}^{X*}|/n$), (d) machine currents i_a, i_b, and i_c, (e) cluster currents i_a^P, i_a^N, etc., and (f) circulating currents i_α^Σ and i_β^Σ.

1) Nominal Flux Operation: The rotational speed and the d-axis current obtained in this test are shown in Fig. 14(a) and (b), respectively. The speed is changed from $\omega_r = 0$ r/min to $\omega_r = 2000$ r/min and then reversed to $\omega_r = -2000$ r/min at $t \approx 13$ s. Although the LFM algorithm considers the fluctuations in the total cluster voltages to calculate $\mathbf{v}_{Cdq}^{\Delta*}$, the individual cell capacitor voltages are well regulated. This is shown in Fig. 14(c). Each capacitor voltage is inside the threshold $|\tilde{v}_{Cx}^{X*}|/n$ over the whole frequency range. As discussed in Section III-B, the circulating currents [see Fig. 14(f)] decrease as the magnitude of

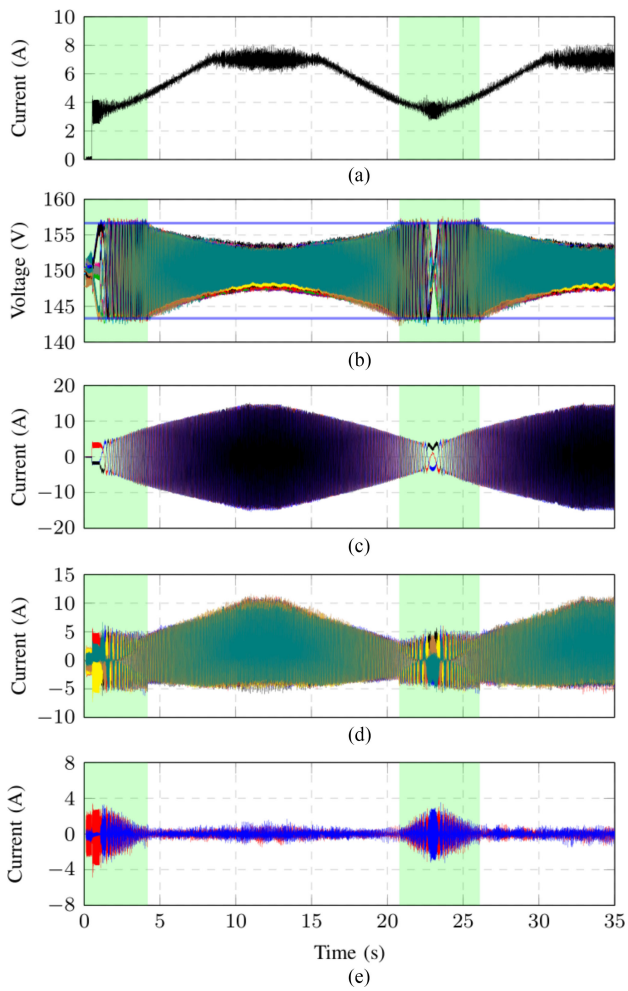

Fig. 15. Experimental results during flux-weakening operation. (a) d-axis current i_d, (b) capacitor voltages v_{Ca1}^P, v_{Ca2}^P, etc. (the blue lines represent $|\tilde{v}_{Cx}^{X*}|/n$), (c) machine currents i_a, i_b, and i_c, (d) cluster currents i_a^P, i_a^N, etc., and (e) circulating currents i_α^Σ and i_β^Σ.

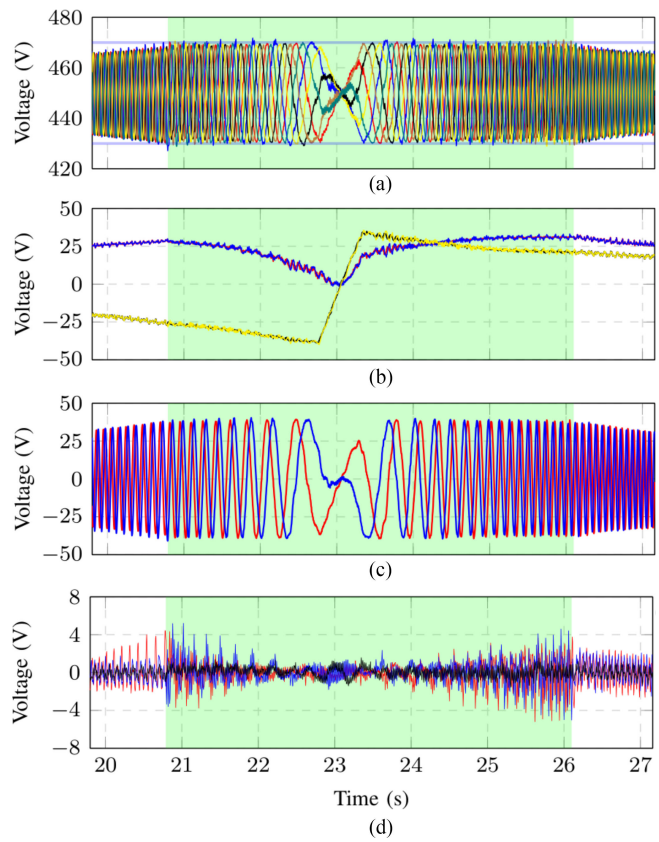

Fig. 16. Controlled variables during flux-weakening operation. (a) total cluster voltages ($PNabc$-coordinates), total cluster voltages ($\Sigma\Delta\alpha\beta 0$-coordinates); (b) v_{Cd}^Δ (red), $v_{Cd}^{\Delta *}$ (blue), v_{Cq}^Δ (black), and $v_{Cq}^{\Delta *}$ (yellow); (c) $v_{C\alpha}^\Delta$ and $v_{C\beta}^\Delta$; and (d) $v_{C\alpha}^\Sigma$ (red), $v_{C\beta}^\Sigma$ (blue), and v_{C0}^Δ (black).

the machine frequency increases, allowing a fast and seamless transition between the operating modes. In fact, the maximum value of $\mathbf{i}_{\alpha\beta}^\Sigma$ occurs when $\omega_e \approx 0$ rad·s^{-1}, because the influence of the vector $\mathbf{p}_m$ is negligible at this point [see (12)]. Due to this feature, the clusters can be designed considering the machine nominal current, since the peak value of the cluster currents is obtained at full load, as depicted in Fig. 14(d) and (e).

2) Flux-Weakening Operation: In Fig. 15, experimental results considering flux-weakening operation are shown. For this test, the same speed and load profile, used to obtain the experimental results shown in Fig. 14, are considered. The resulting d-axis current, is depicted in Fig. 15(a). Unlike conventional flux-weakening algorithms, in the proposed control system the flux is reduced in the low-speed region. Fig. 15(b) shows the corresponding regulation of the capacitor voltages that are maintained inside the predefined threshold during the whole operating range. Moreover, the transition between modes is again seamless and achieved with fast dynamics. The main advantage of the proposed flux-weakening algorithm is that the circulating currents are reduced (during LFM operation) by about 50% when the experimental results shown in Fig. 15(e) are compared with those of Fig. 14(f). This reduction affects the cluster currents as shown in Fig. 15(d). Therefore, the losses in an MMC-based drive could be reduced if flux-weakening operation is feasible, such as for quadratic torque-speed profiles. Moreover, the range where the LFM is active has been reduced by 20% (from $\Delta t \approx 6.62$ s to $\Delta t \approx 5.33$ s), implying that a more efficient use of the common-mode voltage v_0 and circulating current $\mathbf{i}_{\alpha\beta}^\Sigma$ is achieved during the speed profile shown in Fig. 14(a).

In Fig. 16, additional results for flux-weakening operation are shown. These correspond to an amplified view of some variables during zero-crossing of the speed (close to $t = 23$ s in Fig. 15). The total cluster voltages are shown in Fig. 16(a). Notice that the voltages are inside the predefined threshold, even during the transition between modes. The regulation of $\mathbf{v}_{Cdq}^\Delta$ is shown in Fig. 16(b). It is performed with an excellent dynamic response and good tracking of the set-point value $\mathbf{v}_{Cdq}^{\Delta *}$, which has been linearly reduced close to $\omega_e = 0$ rad·s^{-1} to avoid chattering at low speeds [see (19)]. This is not a drawback of the proposed methodology since the influence of $\mathbf{p}_m$ is reduced at $\omega_e \approx 0$ rad·s^{-1}. Finally, as discussed in Section III-B, the fluctuations in the total cluster voltages are dominated by $\mathbf{v}_{C\alpha\beta}^\Delta$ [see Fig. 16(c)]. The fluctuations in the other $\Sigma\Delta\alpha\beta 0$-voltages are small and are well regulated, as shown in Fig. 16(d).

VI. Conclusion

This paper demonstrated that a holistic control system design approach, considering the dynamics of the converter and cage induction machine, is advantageous to enhance the performance and design of MMC-based drives. Flux-weakening operation and the proposed control system to maintain the capacitor voltages inside a predefined threshold are beneficial as demonstrated in this paper. Furthermore, the proposed control scheme allows a seamless transition between the drive operating modes. One of the possible disadvantages of the proposed methodology is higher complexity that is translated into a higher computational burden. For instance, for flux-weakening operation, the variations in the magnetizing inductance and rotor time constant of the induction machine have to be calculated offline and stored in a lookup table, in order to maintain proper rotor flux orientation of the indirect rotor-flux vector control system during the whole speed operating range. However, even with this additional complexity, the proposed control system is relatively simple to implement in a modern digital signal processor augmented with FPGA platforms.

Extensive experimental results from a laboratory prototype were presented in the paper. Experimental tests were conducted under both steady-state and dynamic conditions for both operating modes. The performance considering ramp variations in the speed, flux-weakening operation, different loading conditions, and zero-crossing speed transitions were experimentally investigated and good performance was demonstrated. The experimental results have demonstrated the effectiveness of the proposed strategies.

References

[1] R. Marquardt, "Stromrichterschaltungen mit verteilten energiespeichern," German Patent DE20 122 923 U1, 2001.

[2] M. Glinka and R. Marquardt, "A new AC/AC-multilevel converter family applied to a single-phase converter," in *Proc. 5th Int. Conf. Power Electron. Drive Syst.*, Nov. 2003, vol. 1, pp. 16–23, doi: 10.1109/PEDS.2003.1282669.

[3] M. Saeedifard and R. Iravani, "Dynamic performance of a modular multilevel back-to-back HVDC system," *IEEE Trans. Power Del.*, vol. 25, no. 4, pp. 2903–2912, Oct. 2010, doi: 10.1109/TPWRD.2010.2050787.

[4] Siemens. "HVDC PLUS-basics and principle of operation," 2013. [Online]. Available: http://www.energy.siemens.com/br/pool/br/transmissao-de-energia/transformadores/hvdc-plus-basics-and-principle-of-operation.pdf

[5] S. Debnath, J. Qin, B. Bahrani, M. Saeedifard, and P. Barbosa, "Operation, control, and applications of the modular multilevel converter: A review," *IEEE Trans. Power Electron.*, vol. 30, no. 1, pp. 37–53, Jan. 2015, doi: 10.1109/TPEL.2014.2309937.

[6] Y. Okazaki *et al.*, "Experimental comparisons between modular multilevel DSCC inverters and TSBC converters for medium-voltage motor drives," *IEEE Trans. Power Electron.*, vol. 32, no. 3, pp. 1805–1817, Mar. 2017, doi: 10.1109/TPEL.2016.2562103.

[7] K. Ilves, L. Bessegato, and S. Norrga, "Comparison of cascaded multilevel converter topologies for AC/AC conversion," in *Proc. Int. Power Electron. Conf.*, May. 2014, pp. 1087–1094, doi: 10.1109/IPEC.2014.6869722.

[8] M. Hagiwara, K. Nishimura, and H. Akagi, "A medium-voltage motor drive with a modular multilevel PWM inverter," *IEEE Trans. Power Electron.*, vol. 25, no. 7, pp. 1786–1799, Jul. 2010, doi: 10.1109/TPEL.2010.2042303.

[9] N. Thitichaiworakorn, M. Hagiwara, and H. Akagi, "Experimental verification of a modular multilevel cascade inverter based on double-star bridge cells," *IEEE Trans. Ind. Appl.*, vol. 50, no. 1, pp. 509–519, Jan. 2014. doi: 10.1109/TIA.2013.2269896.

[10] M. Hagiwara, I. Hasegawa, and H. Akagi, "Start-up and low-speed operation of an electric motor driven by a modular multilevel cascade inverter," *IEEE Trans. Ind. Appl.*, vol. 49, no. 4, pp. 1556–1565, Jul./Aug. 2013, doi: 10.1109/TIA.2013.2256331.

[11] A. J. Korn, M. Winkelnkemper, and P. Steimer, "Low output frequency operation of the modular multi-level converter," in *Proc. IEEE Energy Convers. Congr. Expo.*, Sep. 12–16, 2010, pp. 3993–3997, doi: 10.1109/ECCE.2010.5617802.

[12] A. Antonopoulos, L. Ängquist, S. Norrga, K. Ilves, L. Harnefors, and H.-P. Nee, "Modular multilevel converter AC motor drives with constant torque from zero to nominal speed," *IEEE Trans. Ind. Appl.*, vol. 50, no. 3, pp. 1982–1993, May 2014, doi: 10.1109/TIA.2013.2286217.

[13] A. Antonopoulos, L. Ängquist, L. Harnefors, and H. P. Nee, "Optimal selection of the average capacitor voltage for variable-speed drives with modular multilevel converters," *IEEE Trans. Power Electron.*, vol. 30, no. 1, pp. 227–234, Jan. 2015, doi: 10.1109/TPEL.2014.2316273.

[14] J. Kolb, F. Kammerer, M. Gommeringer, and M. Braun, "Cascaded control system of the modular multilevel converter for feeding variable-speed drives," *IEEE Trans. Power Electron.*, vol. 30, no. 1, pp. 349–357, Jan. 2015, doi: 10.1109/TPEL.2014.2299894.

[15] M. Espinoza, E. Espina, M. Diaz, A. Mora, and R. Cárdenas, "Improved control strategy of the modular multilevel converter for high power drive applications in low frequency operation," in *Proc. 18th Eur. Conf. Power Electron. Appl.*, Karlsruhe, Germany, Sep. 2016, pp. 5–9, doi: 10.1109/EPE.2016.7695557.

[16] M. Espinoza, R. Cárdenas, M. Díaz, and J. C. Clare, "An enhanced dq-Based vector control system for modular multilevel converters feeding variable-speed drives," *IEEE Trans. Ind. Electron.*, vol. 64, no. 4, pp. 2620–2630, Apr. 2017, doi: 10.1109/TIE.2016.2637894.

[17] B. Li *et al.*, "An improved circulating current injection method for modular multilevel converters in variable-speed drives," *IEEE Trans. Ind. Electron.*, vol. 63, no. 11, pp. 7215–7225, Nov. 2016, doi: 10.1109/TIE.2016.2547899.

[18] D. E. Soto-Sanchez, R. Pena, R. Cardenas, J. Clare, and P. Wheeler, "A cascade multilevel frequency changing converter for high-power applications," *IEEE Trans. Ind. Electron.*, vol. 60, no. 6, pp. 2118–2130, Jun. 2013, doi: 10.1109/TIE.2012.2194971.

[19] Siemens. SINAMICS SM120 Cabinet Modules. July 2016. [Online]. Available: https://www.industry.siemens.com/drives/global/en/converter/mv-drives/Pages/sinamics-sm120-cm.aspx

[20] B. Li, S. Zhou, D. Xu, D. Xu, and W. Wang, "Comparative study of the sinusoidal-wave and square-wave circulating current injection methods for low-frequency operation of the modular multilevel converters," in *Proc. IEEE Energy Convers. Congr. Expo.*, Sep. 2015, pp. 4700–4705, doi: 10.1109/ECCE.2015.7310324.

[21] R. Cardenas, R. Pena, G. M. Asher, J. Clare, and R. Blasco-Gimenez, "Control strategies for power smoothing using a flywheel driven by a sensorless vector-controlled induction machine operating in a wide speed range," *IEEE Trans. Ind. Electron.*, vol. 51, no. 3, pp. 603–614, Jun. 2004, doi: 10.1109/TIE.2004.825345.

[22] Y. Okazaki, H. Matsui, M. M. Muhoro, M. Hagiwara, and H. Akagi, "Enhancement on capacitor-voltage-balancing capability of a modular multilevel cascade inverter for medium-voltage synchronous-motor drives," in *Proc. IEEE Energy Convers. Congr. Expo.*, Sep. 2015, pp. 6352–6359, doi: 10.1109/ECCE.2015.7310550.

[23] M. Espinoza, R. Cárdenas, M. Diaz, A. Mora, and S. D, "Modelling and control of the modular multilevel converter in back to back configuration for high power induction machine drives," in *Proc. 42nd Annu. Conf. IEEE Ind. Electron. Soc.*, Florence, Italy, Oct. 2016, pp. 24–27, doi: 10.1109/IECON.2016.7793979

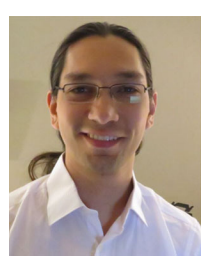

Mauricio Espinoza-B. (S'15) was born in Alajuela, Costa Rica. He received the B.S. and Lic. degrees in electrical engineering from the University of Costa Rica, San Pedro, Costa Rica, in 2010 and 2012, respectively. He is currently working toward the Ph.D. degree in electrical engineering with the University of Chile, Santiago, Chile.

From 2010 to 2014, he was a Lecturer with the University of Costa Rica. During his career, he has worked in research projects related to modular multilevel converters, machine modelling, and control systems for power electronics.

Roberto Cárdenas (S'95–M'97–SM'07) was born in Punta Arenas, Chile. He received the B.S. degree from the University of Magallanes, Punta Arenas, Chile, in 1988, and the M.Sc. and Ph.D degrees from the University of Nottingham, Nottingham, U.K., in 1992 and 1996, respectively, all in electrical and electronic engineering.

From 1989 to 1991 and 1996 to 2008, he was a Lecturer with the University of Magallanes. From 1991 to 1996, he was with the Power Electronics Machines and Control Group, University of Nottingham. From 2009 to 2011, he was with the Electrical Engineering Department, University of Santiago. He is currently a Professor of Power Electronics and Drives with the Electrical Engineering Department, University of Chile, Santiago, Chile. His main research interests include control of electrical machines, variable speed drives, and renewable energy systems.

Jon Clare (M'90–SM'04) was born in Bristol, U.K., in 1957. He received the B.Sc. and Ph.D. degrees in electrical engineering from the University of Bristol, Bristol, U.K.

From 1984 to 1990, he was a Research Assistant and Lecturer with the University of Bristol, where he was involved in teaching and research on power electronic systems. Since 1990, he has been with the Power Electronics, Machines and Control Group, The University of Nottingham, Nottingham, U.K., where he is currently a Professor of Power Electronics. His research interests include power-electronic converters and modulation strategies, variable-speed-drive systems, and electromagnetic compatibility.

Prof. Clare is a holder of the Royal Society Wolfson Research Merit Award (2016-2021).

Diego Soto-Sanchez (M'95) received the B.Sc. degree in electrical engineering from the University of Magallanes, Punta Arenas, Chile, in 1989, and the Ph.D. degree in electrical engineering from Imperial College of London, London, U.K., in 1999.

Since 1999, he has been a Lecturer with the University of Magallanes, where he is involved in teaching and research in Power Electronics and Drives. From 2010 to 2012, he was also a Research Associate with the Control and Power Group, Imperial College London. His research interests include large power converters for power system applications such as FACTS and HVDC.

Matias Diaz (S'15) was born in Santiago, Chile. He received the B.Sc. and M.Sc. degrees in electrical engineering from the University of Santiago of Chile, Chile, in 2011, and the Ph.D. degree in electrical and electronic engineering from the University of Nottingham, Nottingham, U.K., and in electrical engineering from the University of Chile, Santiago, Chile, in 2017.

From 2013 to 2015, he was the Subdirector of the School of Engineering, Duoc-UC, Chile. Currently, he is an Assistant Professor with the University of Santiago, Santiago, Chile. His main research interests include the control of wind energy conversion systems and multilevel converters.

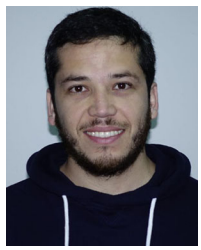

Enrique Espina (S'17) was born in Santiago, Chile. He received the B.Sc. degree in electrical engineering from the University of Santiago of Chile, Santiago, Chile, in 2012, and the M.Sc. degree in electrical engineering from the University of Chile, Santiago, Chile, in 2017, where he is currently working toward the Ph.D. degree in electrical engineering.

Since 2017, he has been a part-time Lecturer with the Department of Electrical Engineering, University of Santiago of Chile. His main research interests include the control of hybrid microgrids, renewable systems, and power electronic converters.

Christoph M. Hackl (M'12–SM'16) was born in 1977, in Mannheim, Germany. He received the B.Sc., Dipl. Ing., and Dr. Ing. (Ph.D.) degrees in electrical engineering from the Technical University of Munich (TUM), Munich, Germany, in 2003, 2004, and 2012, respectively.

Since 2004, he has been teaching Electrical Drives, Power Electronics, and Mechatronic and Renewable Energy Systems, in Technische Universität München. Since 2014, he has been heading the Research Group "Control of Renewable Energy Systems (CRES)" with TUM. In February 2018, he has been appointed as a Professor for Electrical Machines and Drives with the Munich University of Applied Sciences, Munich, Germany. His main research interests include nonlinear, adaptive and optimal control of electric, mechatronic, and renewable energy systems.